Acta Materialia 99 (2015) 259–272

Contents lists available at ScienceDirect

Acta Materialia

journal homepage: www.elsevier.com/locate/actamat

The effect of Sn concentration on oxide texture and microstructure formation in zirconium alloys

Alistair Garner [a,*], Jing Hu [b], Allan Harte [a], Philipp Frankel [a], Chris Grovenor [b], Sergio Lozano-Perez [b], Michael Preuss [a]

[a] Materials Performance Centre, School of Materials, The University of Manchester, Manchester M13 9PL, UK
[b] Department of Materials, Oxford University, Parks Road, Oxford OX1 3PH, UK

ARTICLE INFO

Article history:
Received 8 April 2015
Accepted 1 August 2015
Available online 14 August 2015

Keywords:
Zirconium oxide
Texture
Microstructure
TEM
EBSD

ABSTRACT

The development of oxide texture and microstructure formed on two zirconium alloys with differing Sn contents (Zr–1Nb–1Sn–0.1Fe, i.e. ZIRLO™ and Zr–1.0Nb–0.1Fe) has been investigated using transmission Kikuchi diffraction (TKD) in the scanning electron microscope (SEM) and automated crystal orientation mapping in the transmission electron microscope (TEM). Bulk texture measurements were also performed using electron backscatter diffraction (EBSD) in order to quantify and compare the oxide macrotexture development. The Sn-free alloy showed significantly improved corrosion performance by delay of the transition region and reduced levels of hydrogen pickup. The macroscopic texture and grain misorientation analysis of the oxide films showed that the improved corrosion performance and reduced hydrogen pick up can be correlated with increased oxide texture strength, the improved oxide grain alignment resulting in longer, more protective columnar grain growth. A lower tetragonal phase fraction is also observed in the Sn-free alloy. This results in less transformation to the stable monoclinic phase during oxide growth, which leads to reduced cracking and interconnected porosity and also to the formation of larger, well-aligned monoclinic grains. It is concluded that the Zr–1.0Nb–0.1Fe alloy is more resistant to hydrogen pickup due the formation of a denser oxide with a larger columnar grain structure.

1. Introduction

Ever since the development of the first zirconium alloy, Zircaloy-1, which was alloyed with 2.5% Sn, a reduction in Sn content has been correlated with improved corrosion performance [1–4]. However, this improvement is coupled with a reduction in creep resistance and yield stress [5] and therefore modern Nb-containing Zr alloys contain small amounts of Sn in order to maintain adequate mechanical properties. There have been numerous studies providing evidence that alloys with reduced levels of Sn exhibit a low tetragonal phase fraction in the oxide film [2–4,6]. A recent study [4] has suggested that Sn enables the stress stabilization of the tetragonal phase, and therefore induces increased transformation to the stable monoclinic phase during later stages of oxide growth. The large shear strain and volume expansion associated with this transformation has previously been postulated to cause cracking and porosity in the oxide and to lead to the onset of accelerated corrosion kinetics [7–10]. It has also been suggested that Sn segregation to oxide grain boundaries and the subsequent expansion during oxidation could induce transformation and create porosity at the oxide grain boundaries [3].

The crystallographic orientation of oxide grains that form during corrosion of zirconium alloys has previously been shown to affect the corrosion properties of the oxide. Glavicic demonstrated by X-ray diffraction (XRD) analysis that as the oxide texture strength was increased on a Zr-2.5% Nb alloy, there was a reduction in both oxidation rate and hydrogen pickup [11]. Yilmazbayhan et al. used TEM to show qualitatively that alloys with improved corrosion performance showed a higher proportion of well-aligned columnar monoclinic grains [12]. This relationship between grain orientation and corrosion performance is thought to be due to the fact that well aligned oxide grains should exhibit a high fraction of coherent grain boundaries, and the diffusivity along these grain boundaries is related to their interfacial energy [13]. A number of studies have also indicated that oxide grain boundaries are likely paths for hydrogen through the protective oxide [14–17]. TEM studies have shown interconnected porosity at oxide grain boundaries [9,18], which could provide a transport mechanism for hydrogen through the oxide. This is supported by recent atom probe tomography observations of deuterium

* Corresponding author.

http://dx.doi.org/10.1016/j.actamat.2015.08.005
1359-6454/

enrichment at oxide grain boundaries in samples exposed to heavy water [17].

A strong texture has been observed via XRD [19,20] and TEM [12,21] analysis to form in the monoclinic oxide during corrosion. The formation of this texture in conventionally processed single-phase zirconium alloys is thought to be driven by the transformation stress induced by the zirconium-zirconia transformation [20,22]. The oxide orientations which occupy the smallest in-plane surface area will grow preferentially as they minimise the compressive stress that arises during oxidation of the metal [22]. Therefore a fibre texture is formed with the $(1\,0\,\bar{3})$–$(1\,0\,\bar{5})$ planes oriented parallel with the sample surface [19,20,23]. A (0 0 1) fibre texture has also been observed using XRD to form in the tetragonal phase of oxidised Zircaloy-4 [23]. The growth of these orientations will also minimise the transformation stress as they have the smallest in-plane surface area. It has previously been suggested that transformation of these favourable tetragonal orientations could lead to the formation of the observed monoclinic texture [10]. However, laboratory XRD measurements of the tetragonal phase rely on the measurement of only a single diffraction peak due to the complex nature of the ZrO_2 diffraction spectrum [20,24]. In addition, microtexture measurements rely on the preparation of electron transparent samples, which results in the transformation of the majority of the tetragonal grains [10,25]. Precise measurement of the orientation of the tetragonal grains is therefore difficult with these techniques.

The present study focuses on a comparison between the commercial alloy ZIRLO™ and an experimental alloy, Zr–1.0Nb–0.1Fe developed by Westinghouse, which has the same composition except that no Sn was added to the alloy (Table 1). A previous study has shown a similar distribution of monoclinic $(\bar{1}\,1\,1)$ poles in the oxide formed on these alloys as measured by laboratory XRD [4], however only a single contoured pole figure is presented from each alloy in the pre-transition region and therefore a more detailed analysis of the effect of Sn on oxide texture formation is required. The aim of the present study was to investigate the effect of Sn reduction on oxide texture formation and microstructure development and to link this to the corrosion performance of the alloys, both in terms of oxidation and hydrogen pickup. The complementary use of conventional EBSD, transmission Kikuchi diffraction (TKD) and the automated crystal orientation mapping TEM technique allows for analysis of a large number of oxide grains [10]. It thus provides a more statistical approach, including texture and misorientation distribution analysis, than conventional TEM techniques [12,21,26,27]. In addition, removal of the outer portion of the oxide via mechanical grinding and polishing, and the subsequent examination with EBSD, allowed for examination of the monoclinic and tetragonal texture evolution whilst maintaining the in-plane stress state in the oxide. The hydrogen pick up behaviour of the alloys was also measured as part of this work in order to determine if the differences in behaviour can be correlated with the degree of oxide texture and type of grain misorientation distribution. Such a correlation would provide evidence for oxide grain boundaries providing a preferential transport route for hydrogen through the protective oxide.

2. Experimental methods

2.1. Sample selection

Two alloys were selected for this study; the commercial alloy, ZIRLO™ (Zr–1Sn–1Sn–0.1Fe), and the developmental alloy, Zr–1.0Nb–0.1Fe, both supplied by Westinghouse. Both alloys were in tube form in the recrystallised condition. The measured composition of the alloys is shown in Table 1. The alloys were exposed to simulated primary water chemistry at 360 °C for a total of 540 days as part of a previous research program (MUZIC-1) [9]. The corrosion kinetics are shown in Fig. 1 and each data point is an average weight gain from at least 5 samples. More detail on the corrosion testing can be found in Ref. [28]. In order to have samples with a similar oxide thickness for comparison, one sample was selected from each alloy (circled on Fig. 1). The ZIRLO™ sample had been exposed for a total of 360 days and had an oxide thickness of ~6.4 μm, as measured by weight gain measurements (1 μm of oxide is equivalent to a weight gain of 15 mg dm^2 [29]). The Zr–1.0Nb–0.1Fe sample had been exposed for a total of 540 days in primary water chemistry and also received an additional exposure to deuterated water for 45 days (for NanoSIMS analysis, which is not covered here). The total oxide thickness after 585 days exposure was ~5.4 μm from weight gain measurements. The exposure to deuterium accounted for only an additional 0.2 μm of oxide growth and is not expected to have caused any changes to the microstructure of the pre-existing oxide.

Table 1
Composition in wt.% of zirconium alloys used in this study, measured by EDF using an inductively coupled plasma atomic emission spectrometer (ICP-AES). Balance is zirconium.

Alloy	Cr	Fe	Nb	Ni	Sn
ZIRLO™	<0.01	0.09	0.87	<0.01	0.92
Zr–1.0Nb–0.1Fe	<0.01	0.08	0.91	<0.01	0.01

The approximate time to the first transition in the corrosion kinetics[1] are labelled on Fig. 1. For ZIRLO™ this region can be estimated from the accelerated corrosion kinetics after transition. For Zr–1.0Nb–0.1Fe, however, this was not possible as there are insufficient data points beyond 300 days of corrosion. The transition region was therefore estimated from comparison of the oxidation kinetics to the oxide microstructure, as will be discussed in more detail later.

2.2. Sample preparation

The samples were prepared for bulk EBSD measurements by sectioning a ~6 × 4 mm piece (with the long direction parallel to the axial direction of the tube) and grinding flat using 4000 grit SiC paper. The use of such a fine grit allowed for the preparation of a flat surface without complete removal of the relatively thin oxide. The samples were subsequently polished in a colloidal silica suspension for an extended period of time to remove the grinding scratches. After polishing, a series of cross sections were produced across the tube length using a focussed ion beam (FIB) instrument in order to measure the thickness of the remaining oxide, as shown in Fig. 2. The oxide removal rate was found to vary significantly from the centre to the outside edge of the tube samples, with very little oxide removed from the centre of the tube and all of the oxide removed at each end. The resulting thickness gradient allowed for the measurement by EBSD of bulk oxide texture as a function of oxide thickness. Electron transparent cross-sectional samples for microtexture analysis were prepared by FIB milling using the in situ lift-out technique [30]. Sample preparation using FIB milling is essential for producing large samples of uniform thickness from oxide/metal composites. The samples were prepared with the axial direction of the tube in the plane of the sample. After thinning, low energy FIB cleaning was performed on the samples, which has been shown to remove the surface regions damaged by the ion beam during preparation [31]. After final thinning the typical foil

[1] Zr alloys are known to exhibit cyclic corrosion kinetics. The corrosion kinetics are initially of parabolic to cubic nature before a point at which the protectiveness of the oxide breaks down causing a transition in corrosion kinetics. At this stage the second cycle starts.

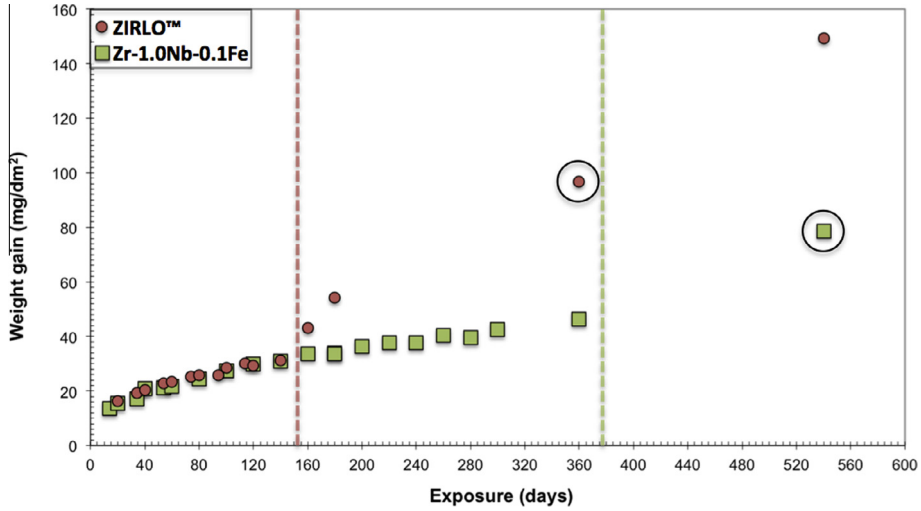

Fig. 1. Corrosion kinetics for ZIRLO™ and Zr–1.0Nb–0.1Fe exposed to simulated primary water chemistry in static autoclave at 360 °C. Approximate first transition regions are indicated by dotted lines and samples selected for investigation are circled.

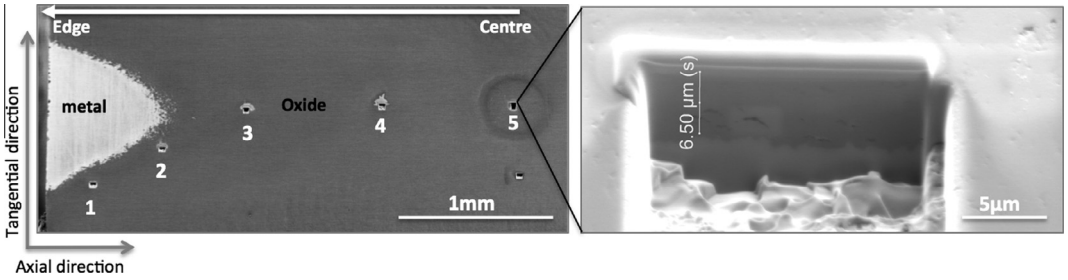

Fig. 2. SEM images showing FIB trenches (numbered) used to measure oxide thickness on ZIRLO™ sample after preparation for EBSD analysis. Oxide thickness reduces from right to left, with the oxide completely removed on the far edge. The image on right shows high magnification image of FIB trench number 5, and shows that the majority of the oxide remains intact in this region, even after extensive grinding and polishing.

thickness was estimated from the electron transparency at low kV in the SEM to be below ~100 nm.

2.3. Electron backscattered diffraction

The EBSD measurements were performed on an FEI Magellan 400 XHR Field Emission Gun Scanning Electron Microscope (FEG-SEM). The use of a FEG source allows for a small spot size with a high current density, which is essential for a nano-grained material such as ZrO_2 formed on a corroded Zr alloy sample. Standard EBSD was employed for the bulk texture measurements using an accelerating voltage of 15 keV and a probe current of 1.6 nA.

2.4. Transmission Kikuchi diffraction

For microtexture measurements, the cross-sectional FIB samples were mounted in transmission geometry in the FEG-SEM and the transmitted Kikuchi patterns were analysed in a technique termed transmission Kikuchi diffraction (TKD) [32], also known as transmission EBSD (t-EBSD) [10]. An accelerating voltage of 30 keV was used with a probe current of 1.6 nA and a step size of 15 nm. The EBSD data was analysed using the Channel 5 software suite developed by Oxford Instruments HKL.

2.5. Automated crystal orientation mapping with TEM

The TEM measurements were performed on an FEI Tecnai F30 Field Emission Gun Transmission Electron Microscope (FEG-TEM) operating at 300 keV. The NanoMEGAS ASTAR automated crystal orientation mapping system was used for both pattern collection and data analysis [33]. The spot patterns were collected by an external CCD camera and matched to theoretically generated patterns using the template matching process [34]. Details of the crystal information used for producing the templates for each phase can be found in Ref. [10]. A small condenser aperture (20 µm) was used in order to reduce the convergence of the beam. The beam size was measured experimentally using the in-column CCD to be ~3 nm with a current of 26 pA. A camera length of 8.9 cm was applied for all measurements with a scanning step size of 5 nm. In addition, a precession angle of 0.8° was used, which produces more diffraction spots and reduces dynamical effects and therefore has been shown to improve the accuracy of the template matching process [33,35].

3. Results

3.1. Hydrogen pickup

Samples from each alloy were selected for hydrogen measurement at various stages in the corrosion process. Hydrogen measurements were performed at Westinghouse Electric Company using a RECO RHEN602 inert gas fusion analyser. The accuracy of hydrogen measurement using this equipment has previously been estimated at ±2% [36], and therefore seems to be more accurate than other methods for hydrogen analysis [37]. The hydrogen concentration as a function of autoclave exposure time is shown in Fig. 3(a). Early in the corrosion process, similar levels of hydrogen concentration are measured in both sets of samples. It should be

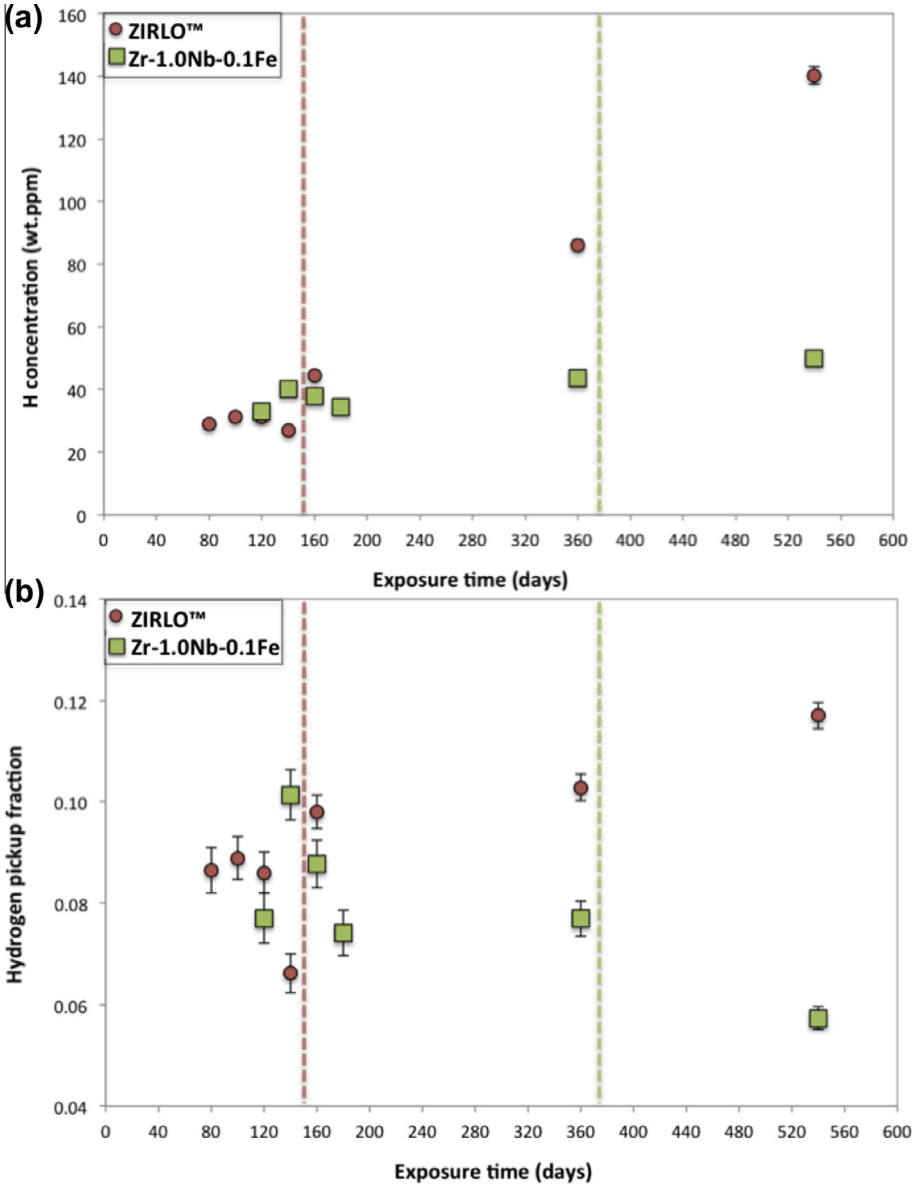

Fig. 3. Hydrogen pickup data for ZIRLO™ and Zr–1.0Nb–0.1Fe, as measured by Westinghouse using the inert gas fusion technique, (a) total hydrogen concentration as a function of exposure time, (b) hydrogen pickup fraction as a function of exposure time. Approximate first transition regions are indicated by dotted lines.

noted that at these low levels of hydrogen, the accuracy of measurement is comparatively poor. Later in the corrosion process, the ZIRLO™ samples pick up significantly more hydrogen than the Sn-free alloy. As the corrosion kinetics of the two alloys are different (Fig. 1), this will affect the amount of available hydrogen liberated by the corrosion reaction. This must be taken into account when comparing hydrogen ingress. Therefore, the hydrogen pickup fraction (HPUF) was estimated, which is the ratio of absorbed hydrogen to the amount of hydrogen generated by corrosion, and is given by [38]:

$$\mathrm{HPUF} = \frac{10^{-6}\left(M_s^t C_H^t - M_s^i C_H^i\right)}{2\frac{M_s^t - M_s^i}{M_O} M_H} \quad (1)$$

where M_s^i and M_s^t are the initial and final masses of the sample respectively, C_H^i and C_H^t are the initial and final hydrogen concentrations respectively and M_O and M_H are the atomic masses of oxygen and hydrogen. The initial hydrogen concentrations were measured prior to autoclave exposure and so the HPUF could be calculated for each hydrogen measurement using the weight gain data. The errors for HPUF were determined using the error propagation formula detailed in Ref. [39]. The HPUF is plotted as a function of exposure time in Fig. 3(b). Early in the corrosion process, both alloys exhibit similar behaviour. The large scatter on these early points is again attributed to difficulties in detecting such low hydrogen concentrations. Later in the corrosion process, the HPUF for ZIRLO™ increases in agreement with previous observations [38]. Zr–1.0Nb–0.1Fe seems to follow a similar trend to the ZIRLO™ until about 200 days of exposure, beyond which it displays significantly lower HPUF. At 540 days, Zr–1.0Nb–0.1Fe exhibits a significant drop in the HPUF to ~6%. This measurement was repeated with a sister sample of the same exposure time, which confirmed the low HPUF at this stage.

3.2. Standard EBSD

A series of EBSD maps were acquired from the oxide of each sample adjacent to the FIB cross sections shown in Fig. 2, which enabled the analysis of the texture as a function of oxide thickness. The scans were carried out using a step size of 120 nm, which is about 3–6 times the width of the columnar oxide grains formed on ZIRLO™ [12,29]. The areas scanned in this way were ~50 × 50 μm. Due to the small grain size and relatively large beam size, and therefore the high probability of the beam probing a grain boundary, the indexing rate was ~40%. However, since each map contained approximately 50,000 indexed points it was possible to measure the representative texture at each oxide thickness. Five maps were collected from each sample adjacent to each of the FIB trenches shown in Fig. 2. An example of a phase map from the region adjacent to FIB trench 2 is shown in Fig. 4, corresponding to a remaining oxide thickness of approximately 1 μm. The map clearly shows the majority of the oxide is monoclinic. In this area, some of the oxide has spalled away revealing the metal underneath.

There are also clusters of tetragonal grains in these thinnest regions, which are postulated to be stress-stabilized tetragonal grains that have previously been shown to exist close to the metal-oxide interface region [29]. It is noted that these clusters of tetragonal grains were only visible in regions of oxide spallation, where the oxide is thinnest. It was also noticed that there was a considerable amount of tetragonal phase indexed in the oxide regions directly adjacent to the FIB trenches. As these large continuous regions of tetragonal grains were seen even in regions of thick oxide where this level of tetragonal phase would not be expected [4], it was concluded that irradiation damage from the FIB had caused local transformation of the monoclinic grains surrounding the trenches. Any maps containing these damaged regions were therefore excluded from this study. Pre-existing tetragonal grains from the corrosion process are also evenly distributed on the maps from thicker oxide regions. The tetragonal phase fraction as a function of approximate distance from the interface is shown for both alloys in Fig. 5. It shows that a higher tetragonal phase fraction is observed in the oxide formed on ZIRLO™ than on Zr–1.0Nb–0.1Fe, with the overall fraction, and the difference between the alloys, increasing closer to the interface, in agreement with previous observations [4,19]. However the tetragonal phase fraction is lower than measured during synchrotron XRD experiments on the same alloys [4]. This is thought to be due to the difficulty in thinning the oxide below ~1 μm without causing spallation, and also due to the fact that a considerable number of the tetragonal grains are below the spatial resolution limit of this technique [12].

A comparison between orientation maps from a region of similar oxide thickness for each alloy are shown in Fig. 6. The maps are coloured according to deviation away from the $(1\,0\,\bar{3})$ fibre component, which has previously been shown to be one of the main fibre components of monoclinic oxide formed during autoclave corrosion [10,23]. The deviation frequency distributions shown in Fig. 6(c) indicate a higher fraction of the monoclinic grains lie within ~10° of this fibre component in the Zr–1.0Nb–0.1Fe sample than in ZIRLO™. There also appears to be a greater proportion of grains oriented away from this component in ZIRLO™. The map also shows that there appear to be regions of well-oriented (blue) monoclinic grains distributed across the oxide surface. These regions could be a result of the previously reported undulations in the metal oxide interface [40]. These undulations would result in the distance to the metal-oxide interface varying at different regions across the sample surface. It is also noted here that this roughness could contribute to the observed spread in the orientations away from the ideal orientation, as the interface will rarely be oriented exactly parallel with the macroscopic sample surface.

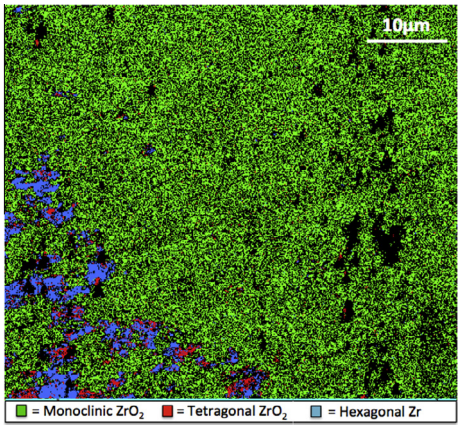

Fig. 4. EBSD phase map taken from region adjacent to FIB trench 2 on ZIRLO™ sample after 360 days autoclave exposure, corresponding to oxide thickness of ~1 μm. Black regions are non-indexed.

In order to quantify the overall texture strength in the monoclinic oxide as a function of oxide thickness, the texture index of each map was calculated. The texture index is the most frequently used method to quantify the degree of preferred orientation in a sample [41]. In this study, it was calculated from the orientation distribution function (ODF) using the open source MATLAB toolbox, MTEX [42]. An alternative quantification of the texture strength is given by the maximum pole figure intensity. Although this does not provide an overall quantification of the texture strength, as the main texture component is already known for this material, it does provide an independent measure of the strength of this texture component. These two quantities, texture index and $(1\,0\,\bar{3})$ pole figure intensity (which in all cases was the pole with the highest intensity) are plotted as function of oxide thickness for ZIRLO™ and Zr–1.0Nb–0.1Fe in Fig. 7. Both quantities are found to be higher throughout the oxide thickness for the Zr–1.0Nb–0.1Fe sample, clearly demonstrating that there is a greater degree of preferred orientation in the monoclinic oxide formed on this alloy. Both samples follow a similar pattern of texture evolution throughout the oxide, with a stronger texture in the outer few microns that decreases in strength towards the interface.

In order to compare the overall distribution of poles, the five maps from each sample were combined. This also allowed for the orientation of a significant number of tetragonal grains to be analysed. Pole figures were plotted from these combined maps using the Channel 5 software suite, and are shown in Figs. 8 and 9. The contoured $(1\,0\,\bar{3})$ pole figures of the monoclinic phase in Fig. 8 show the expected texture, with these planes oriented parallel with the sample surface. These pole figures also show a higher maximum intensity in the oxide formed on Zr–1.0Nb–0.1Fe than in ZIRLO™. It has previously been shown that a (0 0 1) fibre texture is expected in tetragonal zirconia formed on single phase zirconium alloys [23], this being also the orientation with the smallest in-plane surface area. The contoured (0 0 1) tetragonal pole figures shown in Fig. 9 show a similar distribution in the two alloys, with a region of intensity close to the oxide growth direction and also some intensity at approximately 90° to the growth direction. In contrast to the monoclinic phase, the maximum intensity of the tetragonal pole figures is higher in the oxide formed on ZIRLO™. Than on Zr–1.0Nb–0.1Fe. There is a slight misalignment of the central (0 0 1) poles away from the oxide growth direction, this could be a sampling issue due to the comparably small number of grains measured from the tetragonal phase.

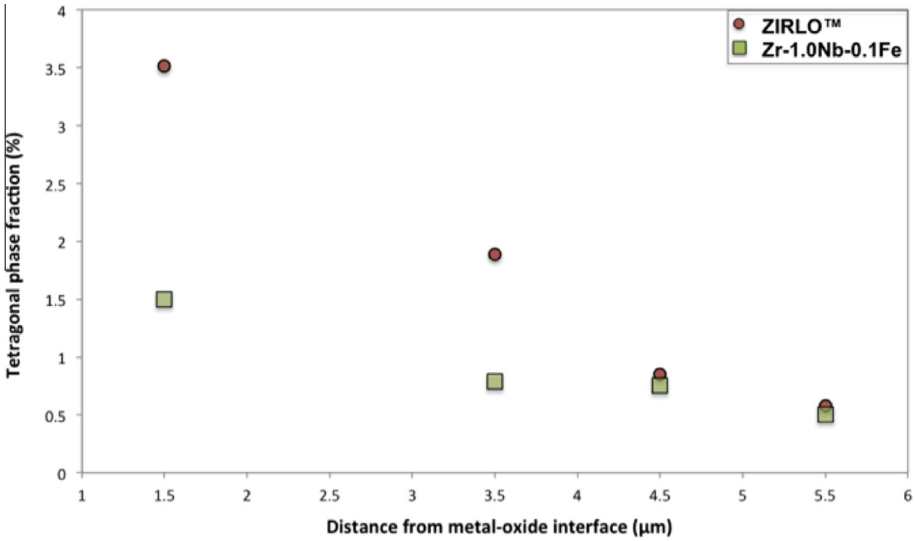

Fig. 5. Tetragonal phase fraction of ZIRLO™ and Zr–1.0Nb–0.0Fe as a function of distance from the metal-oxide interface, as measured by standard EBSD. One map from each sample was excluded from this measurement due to proximity to the FIB trench.

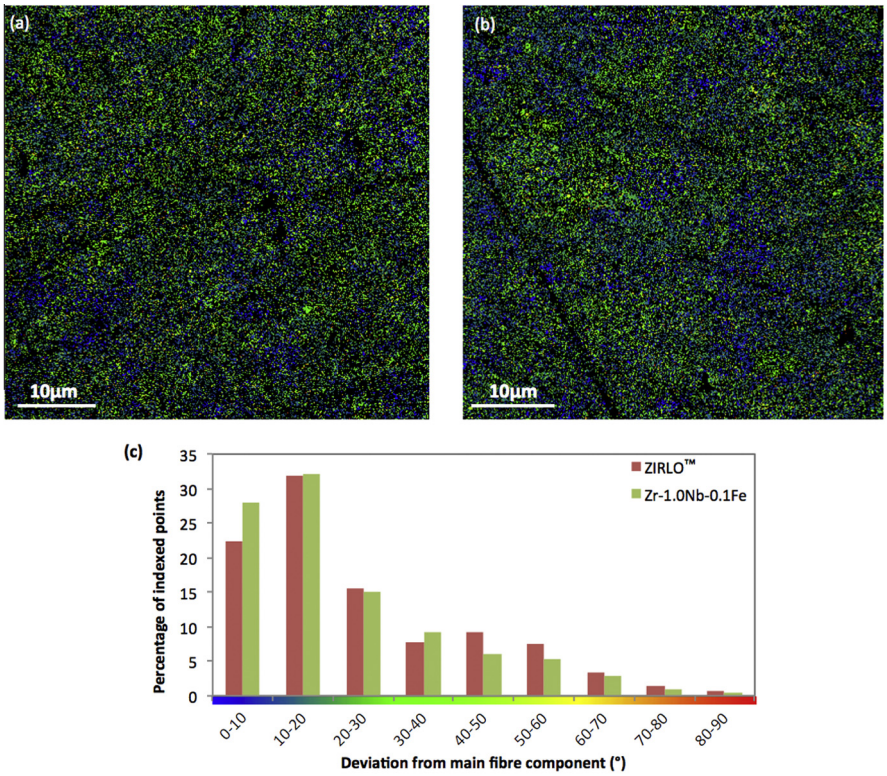

Fig. 6. (a) EBSD monoclinic orientation maps taken from region adjacent to FIB trench 5, corresponding to oxide thickness of ~5 μm. (a) ZIRLO™ and (b) Zr–1.0Nb–0.1Fe. Colouring based on deviation from (1 0 $\bar{3}$) fibre component as shown in (c). Non-indexed points are shown in black. (For interpretation of the references to colour in this figure legend, the reader is referred to the web version of this article.)

3.3. Oxide microstructure

Typical SEM images taken from each of the cross sectional FIB samples can be seen in Fig. 10 and show extensive lateral cracking in both samples. The images display a larger number of lateral cracks in the oxide formed on ZIRLO™ than on Zr–1.0Nb–0.1Fe. In addition, a layer of fine microcracks is clearly visible in the outer ~1 μm of oxide on both samples, which correlates with the equiaxed grain regions seen in the band contrast images plotted from TKD analysis (Fig. 11). These band contrast images also show a more ordered structure in the oxide formed on Zr–1.0Nb–0.1Fe (Fig. 11b) than on ZIRLO™ (Fig. 11a), with clear layers of equiaxed and columnar grains. If it is assumed that the layers of equiaxed grains occur after a transition in the corrosion kinetics when the nucleation rate is fastest, then the positions of these layers can be used to determine when the transitions occurred. It appears that the first lateral cracks appear approximately 1 μm above the

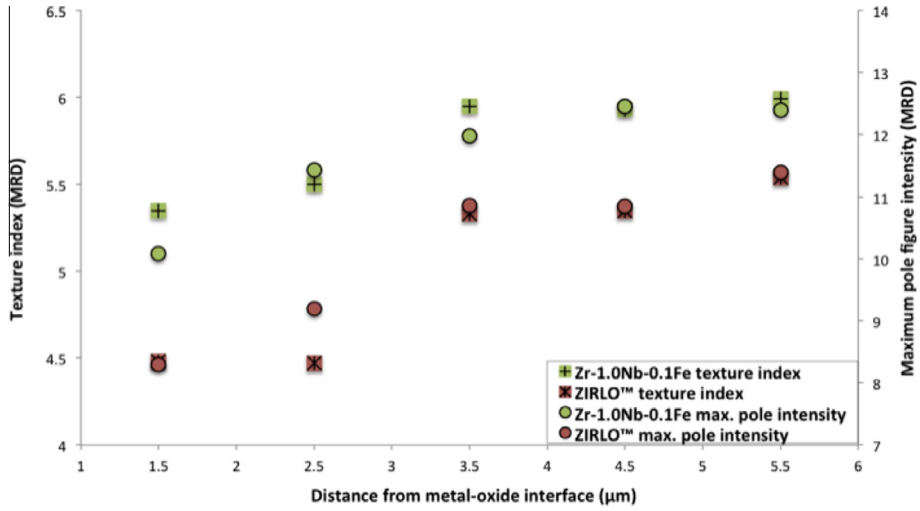

Fig. 7. Monoclinic texture index and maximum monoclinic (1 0 $\bar{3}$) pole figure intensity as a function of oxide thickness for ZIRLO™ and Zr–1.0Nb–0.1Fe, as measured by standard EBSD.

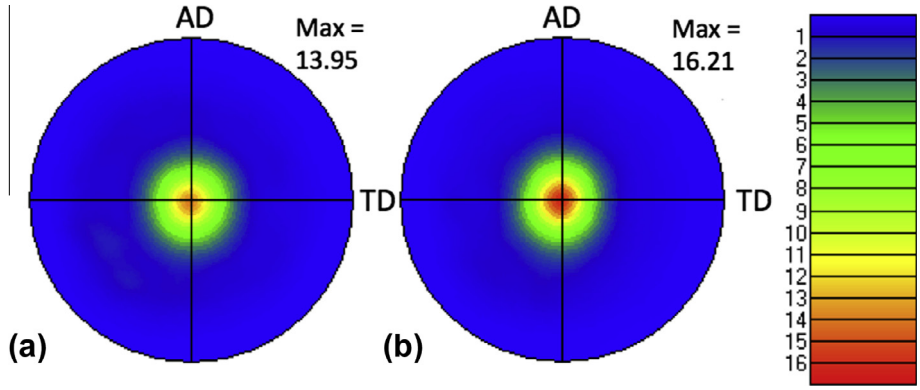

Fig. 8. Contoured (1 0 $\bar{3}$) monoclinic pole figures from combined EBSD maps, (a) ZIRLO™ after 360 days autoclave exposure (280,000 points) and (b) Zr–1.0Nb–0.1Fe after 540 days autoclave exposure (250,000 points).

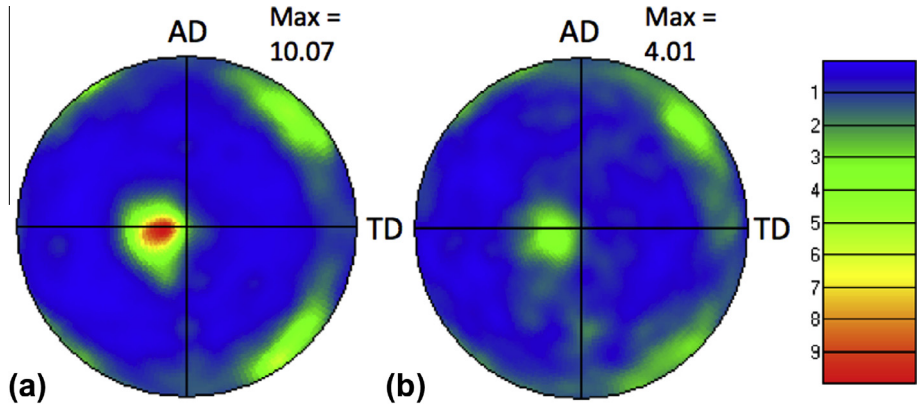

Fig. 9. Contoured (0 0 1) tetragonal pole figures from combined EBSD maps, (a) ZIRLO™ after 360 days autoclave exposure (5000 points) and (b) Zr–1.0Nb–0.1 after 540 days autoclave exposure (2500 points).

equiaxed grain region, these lateral cracks have previously been associated with the transition in corrosion kinetics [43,44]. However, these observations seem to suggest a more gradual development of cracks during the pre and post transition regimes, as observed during 3D characterisation of pre and post transition oxides using FIB sectioning and reconstruction [40].

For Zr–1.0Nb–0.1Fe, there is only one point for this alloy on the corrosion curve after the first transition (Fig. 1), and it is therefore difficult to ascertain exactly when the transition occurs. Interestingly, from the position of the bands of equiaxed grains it appears that the oxide on Zr–1.0Nb–0.1Fe has undergone two transitions after 540 days autoclave exposure. The first transition appears to have occurred at an oxide thickness of ~3 μm

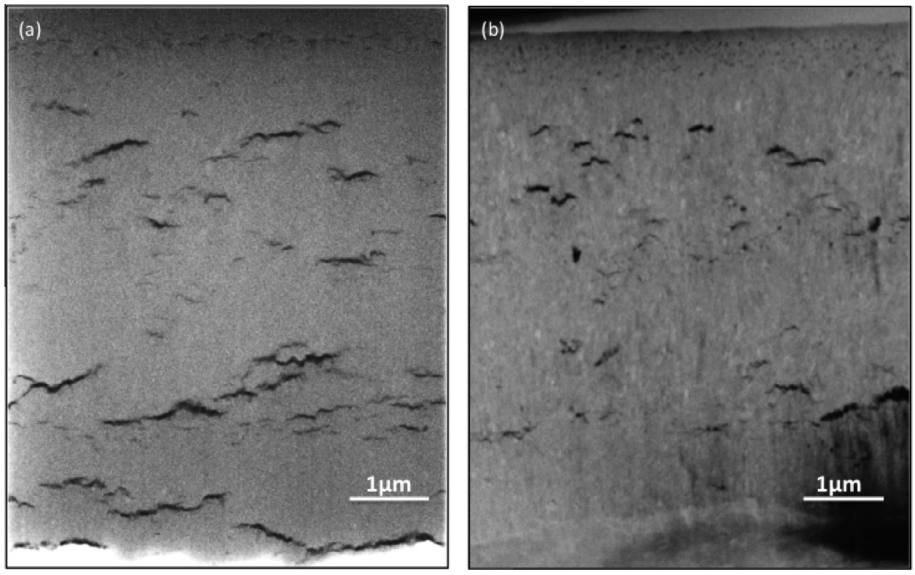

Fig. 10. SEM images showing lateral cracking in oxide formed on (a) ZIRLO™ after 360 days autoclave exposure and (b) Zr–1.0Nb–0.1Fe after 540 days autoclave exposure.

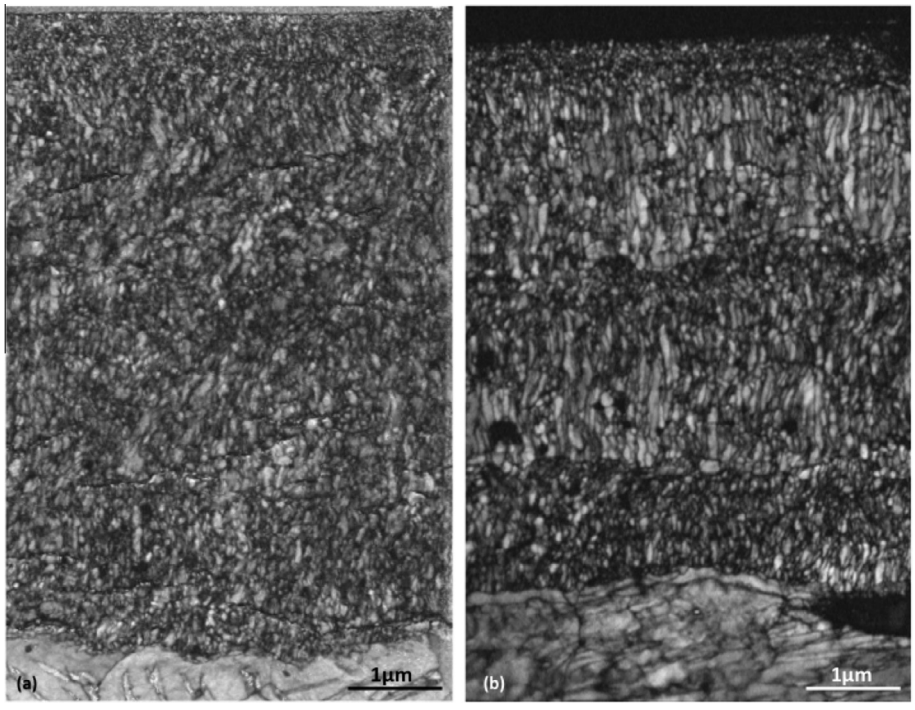

Fig. 11. Band contrast maps measured by transmission Kikuchi diffraction, oxide formed on (a) ZIRLO™ and (b) Zr–1.0Nb–0.1Fe.

(corresponding to an exposure time of ~370 days) and the second appears to occur at an oxide thickness of ~5 μm (corresponding to an exposure time of ~500 days). It is more difficult to infer the transition points from the oxide microstructure formed on ZIRLO™, as the periodic grain structure is not as clear in the band contrast image. There are significant differences in the grain sizes of the oxides formed on the different alloys. From the TKD band structure images in Fig. 11, the length and width of the columnar grains appear to be larger for the oxide formed on Zr–1.0Nb–0.1Fe compared to ZIRLO™. However, it is difficult to quantify the difference in grain size using this technique as the relatively large step size (15 nm) and low indexing rate would lead to inaccurate results. On both samples, the indexed oxide grains are all monoclinic, and no tetragonal phase is detected. This is because the preparation by FIB of the thin TEM samples induces transformation of the larger stress-stabilized tetragonal grains [10], and those that remain in the oxide after sample preparation are therefore postulated to be below the spatial resolution limit of this technique.

In order to provide an accurate quantification of the grain sizes in oxides formed on the two alloys, automated crystal orientation mapping in the TEM was used due to its superior spatial resolution compared to TKD. The reliability index is a measure of the uniqueness of the solution from template matching and therefore will be low at grain boundaries where there are overlapping diffraction patterns [34]. Examples of monoclinic orientation reliability maps

used for grain size analysis are shown in Fig. 12(a) and (b). It is noted that the maps presented here are small representative regions of the recorded maps, and a significantly larger area was used for the grain size analysis. The reliability maps clearly show the wider and longer columnar grains formed on Zr–1.0Nb–0.1Fe compared to ZIRLO™. It is also noted here that only columnar monoclinic grains were included in the grain size analysis, as the small equiaxed grains tend to overlap in the transmission direction and therefore are difficult to measure using this technique. The width and length of the columnar monoclinic grains was measured using the linear intercept method, covering an area of approximately 18 μm^2 on each sample. The average width of the columnar monoclinic grains was measured to be 68 nm and 85 nm on the ZIRLO™ and Zr–1.0Nb–0.1Fe samples respectively. The average length of the columnar monoclinic grains was measured to be 124 nm and 190 nm on the ZIRLO™ and Zr–1.0Nb–0.1Fe samples respectively. The average ZIRLO™ columnar grain width is therefore larger than previously reported using synchrotron XRD (40–45 nm) [29] and conventional TEM (25–33 nm) [12]. However, there are a number of problems associated with measuring grain size accurately using line broadening of X-ray diffraction peaks, especially considering the high levels of residual stress present in the oxide [45]. Also, in the orientation used for standard XRD analysis, the length of the columnar grains does not contribute to the peak broadening. Conventional TEM observations are usually only performed on a small number of grains and so do not have the statistical significance of this study. If these TEM samples are insufficiently thin there might be a bias towards measuring small grain sizes due to overlapping projections of grains along the transmission direction and the greater sensitivity of phase contrast images to low angle grain boundaries. In both of the samples studied here, we measure by bright field TEM in the regions of columnar monoclinic oxide a grain size of ~50 nm. The grain size analysis using the orientation reliability maps is thought to be superior to conventional techniques due to the ability to clearly distinguish grain boundaries from other features. However, it is noted that this technique could be biased towards larger oxide grains due to the difficulties in measuring smaller oxide grains described previously. However the TKD and TEM observations presented here clearly show a significant difference in the monoclinic oxide grain size formed on the two alloys.

3.4. Oxide microtexture

Monoclinic orientation maps, as measured by automated crystal orientation mapping in the TEM, are shown in Fig. 13. As previously mentioned, each solution is given a reliability index, which is a measure of the uniqueness of the solution. This index is an essential part of the analysis of template matching solutions due to the ambiguous nature of high symmetry electron spot patterns. The maps in Fig. 13 therefore only include high reliability solutions. A reliability threshold of 10 has previously been shown to be adequate for monoclinic zirconium oxide [35]. The grains are coloured according to their deviation from the $(1\,0\,\bar{3})$ fibre component, as discussed previously. Qualitatively, it is clear that there are more well aligned columnar grains (blue) in the oxide formed on Zr–1.0Nb–0.1Fe than on ZIRLO™, and that these grains are longer and wider, in agreement with the previous observations. The frequencies of the deviations from the fibre component are shown in Fig. 13(c). In agreement with the EBSD data, there is a significantly higher percentage of indexed points within 10° of the main fibre component in the oxide formed on Zr–1.0Nb–0.1Fe. In the oxide formed on ZIRLO™, there is a wider range of orientations, with a significant number of indexed points lying up to 60° from the $(1\,0\,\bar{3})$ fibre component. It is noted here that the same trend was observed in the TKD orientation data, but is not shown here. Tetragonal grains are highlighted in purple in Fig. 13. A number of small equiaxed tetragonal grains are observed throughout the oxide formed on ZIRLO™, with the total phase fraction in the oxide measured to be ~1%. No tetragonal grains were visible using this technique in the oxide formed on the Sn-free alloy. It is well known that preparation of thin foils for TEM/TKD examination will lead to the transformation of the stress stabilized tetragonal oxide grains [10,31]. However, the grain size stabilized tetragonal grains should remain in the samples and so the fact that none are detected in the Sn-free alloy suggests Sn is affecting the fraction of tetragonal grains that nucleate at the interface. In addition, this observation is supported by the higher tetragonal phase fraction observed on the Sn-containing alloy in this work using bulk EBSD, where the stress state in the oxide is maintained.

The misorientation angle distributions (MADs) for the monoclinic oxide formed on the two alloys as measured using automated crystal orientation mapping with TEM are shown in Fig. 14. The grains in each sample were separated into two groups for MAD analysis; small grains with a equivalent circle diameter of less than 50 nm and large grains with an equivalent circle diameter of greater than or equal to 50 nm. Fig. 14(a) compares the MADs from the smaller monoclinic grains. A similar distribution is observed in the small grains on both alloys, with a large range of misorientation observed between adjacent grains. Fig. 14(b) compares the MADs from the large monoclinic grains and the differences between the alloys become more obvious, with a significantly larger fraction of 90° and 180° boundaries observed in the oxide formed on ZIRLO™ than on Zr–1.0Nb–0.1Fe. These boundaries have previously been shown to be caused by twin variant selection during the martensitic transformation from tetragonal to monoclinic oxide [46,47] and so are evidence of an increased level of phase transformation during oxide growth on ZIRLO™.

4. Discussion

The corrosion kinetics in Fig. 1 demonstrate a clear difference in the oxidation behaviour of the two alloys. The SEM images in Fig. 10 and band contrast images in Fig. 11 can help to identify when the first transition in the corrosion kinetics occurs in the absence of sufficient data points. From analysis of the corrosion kinetics and oxide microstructure, the oxide thicknesses at which the first transition occurs is quite similar between the two alloys. However, the Zr–1.0Nb–0.1Fe alloy takes a significantly longer time to reach this thickness. From extrapolation of the corrosion kinetics in Fig. 1, it would appear that there is approximately a 200 day delay in the first transition for the Zr–1.0Nb–0.1Fe alloy. Thus the oxide formed prior to transition is much more protective for Zr–1.0Nb–0.1Fe than for ZIRLO™. One possible reason for this is the difference in the columnar oxide grain size in the two alloys. The ASTAR observations revealed a columnar grain width/length of 68/124 nm in oxide formed on ZIRLO™, and 85/190 nm on Zr–1.0Nb–0.1Fe. It has previously been demonstrated that the majority of oxygen transport occurs via oxide grain boundaries [48], so the reduced grain boundary area in the oxide formed on Zr–1.0Nb–0.1Fe would result in considerably slower oxidation kinetics. This extended grain growth only becomes significant at an oxide thickness of ~2 μm and therefore the corrosion kinetics of the two alloys are similar in the early stages. A possible reason for the extended growth of these columnar grains is the greater degree of preferred orientation present in this oxide, as shown by the bulk texture measurement in Fig. 7. Motta et al. suggested that the termination of columnar grain growth is caused by small mismatches in the orientation of adjacent grains, causing the accumulation of stress [49]. Therefore, if there is an improved degree of

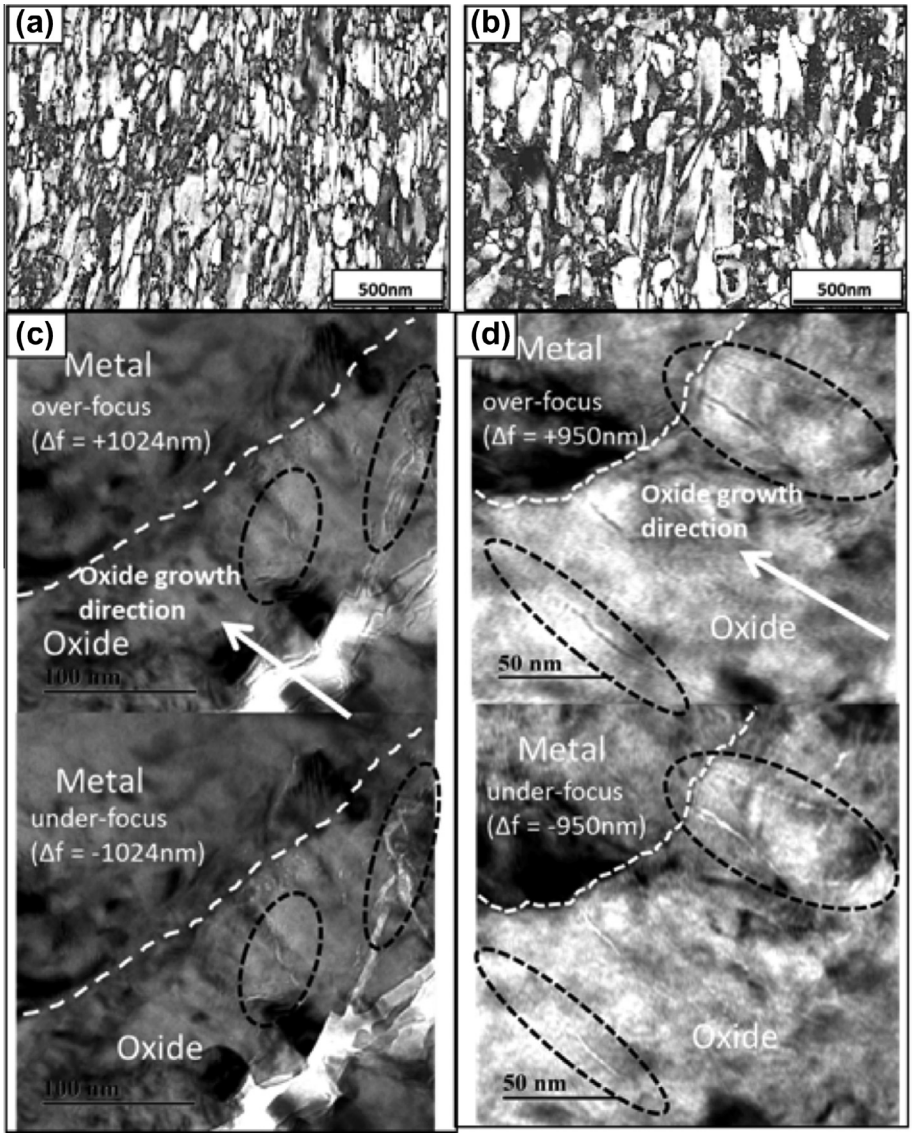

Fig. 12. Monoclinic orientation reliability maps from columnar grain region of oxide formed on (a) ZIRLO™ and (b) Zr–1.0Nb–0.1Fe, measured with automated crystal orientation mapping in TEM. Through-focal imaging of fine pores (circled) at the metal-oxide interface from the oxide formed on (c) ZIRLO™ and (d) Zr–1.0Nb–0.1Fe. Due to Fresnel contrast the porosity changes from dark in the over-focussed images to white in the under-focussed images.

alignment in the growing grains, they will be able to grow further before the intergranular stress caused by the mismatch builds up to the critical level to cause nucleation of new grains.

It is clear from the observations from a number of different experimental techniques shown in this study that the monoclinic oxide formed on Zr–1.0Nb–0.1Fe has a greater degree of preferred orientation than that formed on ZIRLO™. As the alloys followed the same processing route, there is no significant difference in the substrate texture of the alloys. The distribution and nature of intermetallic precipitates will also be similar in the two alloys as their distribution is determined by the level of Nb and Fe in the alloy, which are identical (Table 1). The only difference between the two alloys is therefore the Sn content, which is fully soluble in the matrix and is not found in precipitates. The differences in corrosion behaviour can therefore be attributed to the effect of Sn on oxide formation. A possible mechanism for the increase in oxide texture strength with the removal of Sn is the effect it has on the stability of the tetragonal phase. It is well documented (via non-destructive methods) that a decrease in Sn content results in a lower tetragonal phase fraction [2–4,6]. This is supported by the consistently lower tetragonal phase fraction observed by EBSD in this study on the Zr–1.0Nb–0.1Fe alloy (Fig. 5). It is postulated that Sn^{2+} substitutes for Zr^{4+} in the oxide, causing the production of oxygen vacancies to balance the overall charge [50]. These vacancies are known to stabilize the tetragonal phase [51]. It has also previously been shown that Sn will increase the number of stress-stabilized grains present in the oxide, allowing the grains to grow above the critical size for stabilization [4]. It is therefore likely that these large tetragonal grains are stabilized by a combination of compressive stress in the oxide and also chemical stabilization. A number of studies have clearly shown a reduction in compressive stress as the oxide grows [6,45,52], which could lead to destabilization of these large tetragonal grains. It has also been suggested that the oxidation of Sn during oxide growth will lead to a transformation from Sn^{2+} to Sn^{4+} [50,53,54]. Sn has been observed to exist in both of these valence states experimentally [50,53], with the relative fraction of Sn^{4+} increasing as the oxide thickens [53]. It is therefore possible that the oxidation of Sn during oxide growth is also contributing to the destabilization of the tetragonal phase. This would also explain why the oxides formed

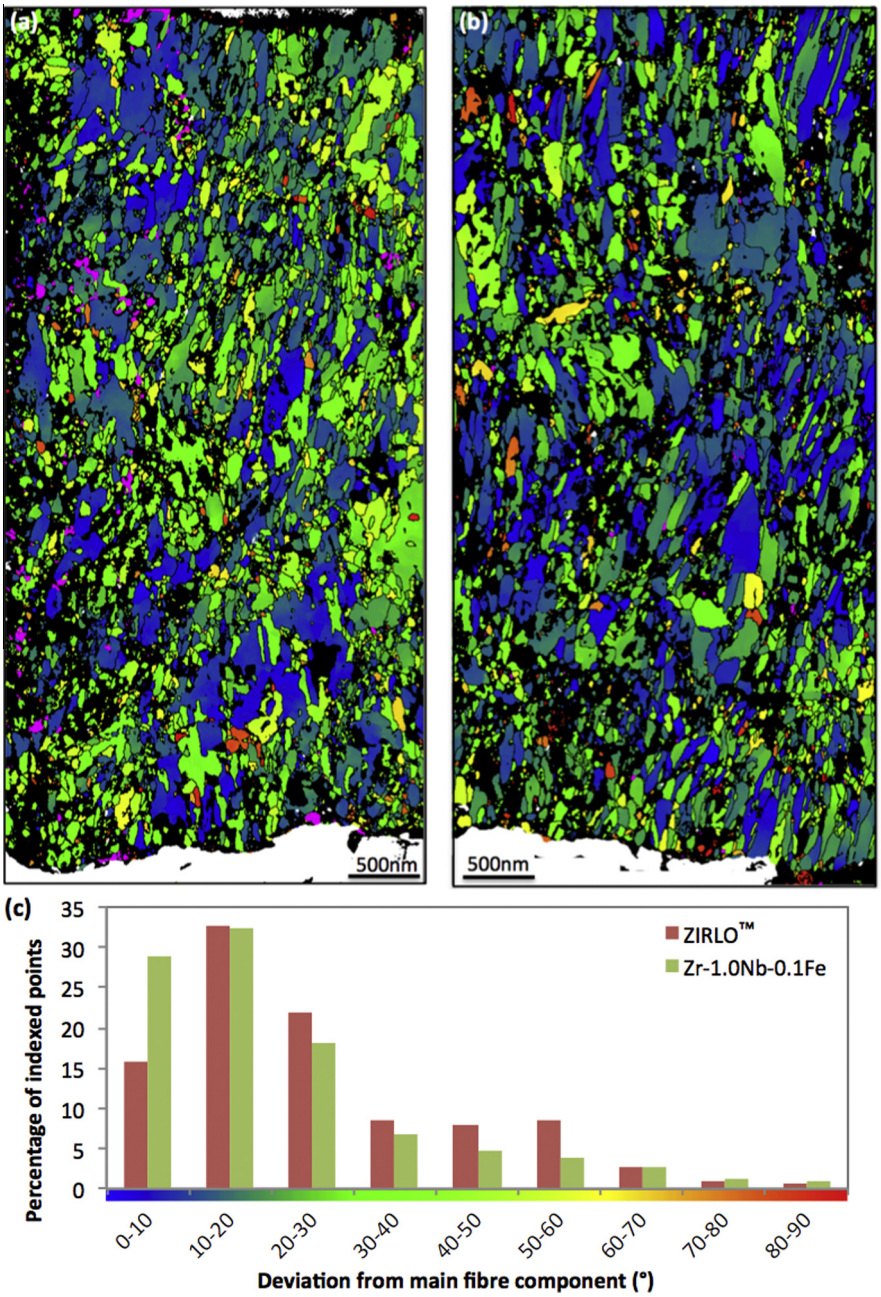

Fig. 13. High reliability (threshold = 10) monoclinic orientation maps measured by automated crystal orientation mapping in TEM. Oxide formed on (a) ZIRLO™ and (b) Zr–1.0Nb–0.1Fe. Coloured according to degrees away from (1 0 $\bar{3}$) fibre component as shown in (c). Tetragonal zirconia grains are shown in purple and zirconium metal grains in white. Black regions are non-indexed. The equiaxed grain region at outer surface has been removed from the maps. (For interpretation of the references to color in this figure legend, the reader is referred to the web version of this article.)

on both alloys show similar tetragonal phase fractions in the oxide ~4 μm away from the metal-oxide interface (Fig. 5), as the Sn in the oxide formed on ZIRLO™ is fully oxidised away from the interface and so has no stabilizing effect on the tetragonal phase.

Therefore in the alloy with higher levels of Sn, the compressive stress that drives the oxide texture formation acts mainly on metastable tetragonal grains [10,20,22]. Consequently when the grains can no longer be stabilized by the surrounding oxide, they will transform to the monoclinic phase according to a specific orientation relationship. Due to the differences in the crystal structures of the two phases, the new phase will no longer be in the preferential orientation, resulting in the greater spread of orientations observed in the oxide on the Sn-containing alloy. Whereas in the alloy with no Sn, the favourable orientations are selected from the stable monoclinic phase, which grow into the large well-oriented columnar grains observed in this work. This argument is supported by the greater degree of preferred orientation observed in the tetragonal phase formed on ZIRLO™, as seen in Fig. 9. Also, a comparison of Figs. 6 and 13 indicates the difference in the preferred orientation of the alloys is different between the bulk EBSD technique (where the stress state in the oxide is largely maintained) and the TEM technique. As the sample preparation for the TEM technique is postulated to cause enhanced transformation of the stress-stabilized tetragonal grains, according to the previous discussion, this would lead to a greater misalignment in the monoclinic phase after transformation, which is observed here.

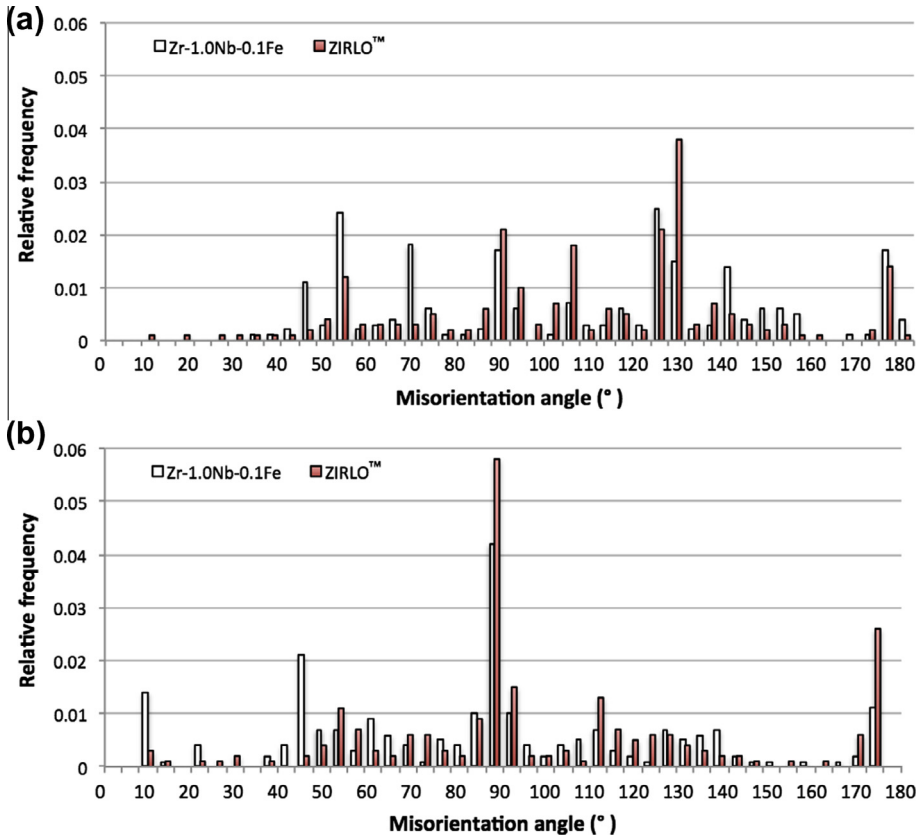

Fig. 14. Comparison of monoclinic misorientation angle distributions from ZIRLO™ and Zr–1.0Nb–0.1Fe as measured by automated crystal orientation mapping in TEM. (a) grain diameter < 50 nm, (b) grain diameter $\geqslant$ 50 nm.

As there is a higher tetragonal fraction in the oxide formed on ZIRLO™ (Fig. 5), it follows that there is more transformation of this phase as the oxide grows. The shear strain and volume expansion associated with this transformation have been associated with the onset of cracking and porosity in the oxide, leading to the breakdown of the protective oxide [7–9]. It is expected that this reduction in transformation will contribute significantly to the improved corrosion performance of the Zr–1.0Nb–0.1Fe alloy. From detailed analysis of the fine scale porosity in the oxides on the two alloys, we have identified a clear difference in the characteristic shape and size of the pores. On the Zr–1.0Nb–0.1Fe alloy the oxide contains almost exclusively isolated spherical pores, often arranged along monoclinic grain boundaries (Fig. 12(d)). By contrast, Fig. 12(c) shows that the ZIRLO™ sample is full of elongated pores (or very fine cracks) that would provide effective interconnection between the larger cracks. Therefore it appears that the increased level of transformation of the tetragonal phase during oxide growth reduces the protectiveness of the oxide and could induce the early onset of transition in Sn-containing alloys.

In addition, the number of lateral cracks in the oxide on the Sn-free sample is significantly reduced compared to ZIRLO™, which could be due to the effect of Sn on the mechanical properties of the substrate. It is well known that Sn strengthens zirconium alloys through solid solution strengthening mechanisms [55]. Therefore, the removal of Sn would be expected to have a significant effect on the mechanical properties of the substrate. It has previously been suggested that interfacial roughness that develops during oxide growth causes the formation of tensile stress regions at the interface which lead to the onset of lateral cracking [44,56]. It is likely that this interfacial roughness forms in order to reduce the stress mismatch at the interface. Therefore, if there is less constraint on the oxide formed on Zr–1.0Nb–0.1Fe, due to the reduction in substrate strength, then there will be less driving force for the development of undulations. This, in turn, will lead to less lateral cracking in oxides formed on alloys with reduced levels of Sn. It is likely that increased levels of lateral cracks will assist in the interconnection of cracks and porosity after transition and so will reduce the protectiveness of the oxide further. As previously mentioned, the roughness of the interface may also affect the spread in the resulting orientations due to the increase in the fraction of the interface that is not parallel with the sample surface. It is therefore possible that a reduced interface roughness may contribute to the formation of a more-well oriented oxide.

It can be seen from Fig. 14 that the removal of Sn also affects the grain boundary distribution in the oxide. As mentioned previously, the columnar monoclinic grains show a greater degree of alignment in the oxide formed on Zr–1.0Nb–0.1Fe. The effect of the alignment of grains on the grain boundary character is likely to affect the diffusion of corrosive species through the oxide, as a low activation energy for diffusion is associated with a high interfacial energy [13]. If the grains are well aligned, then a fairly coherent boundary would be expected to form between adjacent grains which is then more resistant to grain boundary diffusion. In the smaller grains, which are more likely to be un-favourably oriented (Fig. 14(a)), there is a large range of misorientation between adjacent grains, and it is therefore likely that these boundaries are not coherent and therefore not protective. In the larger grains, however there is large fraction of transformation-induced twin boundaries formed on both alloys. These twin boundaries are almost totally coherent, and therefore have very low interfacial energies. These are therefore likely to be more protective than the boundaries between smaller grains and so contribute to the protective nature of columnar grain growth. However, the fact that there is a higher fraction of twin boundaries on the less protective oxide indicates

that it may be the effect of the transformation on the integrity of the oxide, as discussed previously, that is the dominating factor in determining both the oxidation kinetics and pickup of hydrogen.

Concerning the route of hydrogen through the oxide, early in the corrosion process, when the oxides remain largely protective, the H pickup behaviour of the two alloys is similar. In the absence of interconnected cracking and porosity prior to transition, both alloys remain protective against hydrogen ingress and exhibit similar levels of hydrogen pickup. The similarity between these observations and the oxidation kinetics suggests that early in the corrosion process, hydrogen ingress is controlled by diffusion down grain boundaries in the oxide. However, it is clear that the disruption to the oxide caused by the transformation from tetragonal to monoclinic oxide provides easy paths for hydrogen to penetrate the oxide. NanoSIMS observations on isotopically spiked samples have indicated that directly after transition, before the buildup of new protective oxide, the oxide is sufficiently porous to allow for direct contact between the water and metal [57]. This supply of hydrogen close to the interface will reduce the grain boundary length between environment and metal and thus significantly increase the H pickup fraction. This can be seen in the comparison between the H pickup fractions after 360 days of autoclave exposure. Here, the Zr–1.0Nb–0.1Fe alloy, which is considered to still be in the pre-transition regime, remains protective against H ingress. However, the ZIRLO™ sample, which at this stage has undergone more than one transition and therefore contains significant interconnected cracking and porosity, has a larger HPUF. The reason for the dramatic reduction in HPUF in the Zr–1.0Nb–0.1Fe alloy after 540 days autoclave exposure (when the oxide is assumed to have undergone transition) is postulated to be due to reduced levels of interconnected cracking and porosity caused by the low tetragonal phase fraction and also the larger oxide grain size in the dense oxide close to the interface. Therefore the legacy oxide retains a higher degree of protectiveness against both oxidation and hydrogen pickup.

5. Conclusions

A detailed study of the texture and microstructure of oxides formed on two zirconium alloys which exhibit different corrosion behaviour (ZIRLO™ and Zr–1.0Nb–0.1Fe) has been performed in order to investigate the effect of the removal of Sn on oxide texture formation during aqueous corrosion. The following conclusions are made:

- The removal of Sn leads to a delayed transition in the corrosion kinetics (~200 days) and a reduction in hydrogen pickup.
- A greater degree of preferred orientation is present in monoclinic oxide formed on Zr–1.0Nb–0.1Fe, which allows for the growth of larger columnar grains.
- The average columnar grain width and length is larger for the oxide formed on Zr–1.0Nb–0.1Fe and also exhibits a more ordered oxide grain structure.
- A higher tetragonal phase fraction is observed in oxide formed on ZIRLO™, this is attributed to the stabilizing effect of the presence of Sn in the oxide.
- There is more lateral cracking in the oxide formed on ZIRLO™, this is attributed to the effect of Sn on the mechanical properties of the substrate and its influence on the formation of undulations in the metal-oxide interface.
- It is concluded that the improved corrosion performance of Zr–1.0Nb–0.1Fe is due to the reduced stabilization of tetragonal grains in the absence of Sn. This results in the formation of larger, well-oriented columnar grains and leads to less transformation and therefore a delayed transition.
- The combined effect of reduced disruption and increased columnar grain size leads to the Zr–1.0Nb–0.1Fe alloy remaining protective against H ingress, even after 540 days autoclave exposure.

Acknowledgements

This work was conducted as part of the MUZIC-2 collaboration studying hydrogen pickup mechanisms in zirconium alloys. Financial support and fruitful discussions from this community are gratefully acknowledged. Also, this project is financially supported by Rolls-Royce through the Advanced Metallic Systems Centre for Doctoral Training.

References

[1] M. Harada, M. Kimpara, K. Abe, Effect of alloying elements on uniform corrosion resistance of zirconium-based alloys in 360 °C water and 400 °C steam, in: Zirconium in the Nuclear Industry: 9th International Symposium, ASTM STP 1132, 1991, pp. 368–391.
[2] P. Barberis, Zirconia powders and Zircaloy oxide films: tetragonal phase evolution during 400 °C autoclave tests, J. Nucl. Mater. 226 (1995) 34–43.
[3] K. Takeda, H. Anada, Mechanism of corrosion rate degradation due to tin, in: Zirconium in the Nuclear Industry: 12th International Symposium, ASTM STP 1354, 2000, pp. 592–608.
[4] J. Wei, P. Frankel, E. Polatidis, M. Blat, A. Ambard, R.J. Comstock, L. Hallstadius, M. Preuss, The effect of Sn on autoclave corrosion performance and corrosion mechanisms in Zr–Sn–Nb alloys, Acta Mater. 61 (11) (2013) 4200–4214.
[5] G.P. Sabol, ZIRLO – an alloy development success, in: Zirconium in the Nuclear Industry: 14th International Symposium, ASTM STP 1467, 2005, pp. 2–24.
[6] N. Petigny, P. Barberis, C. Lemaignan, V. Ch, M. Lallemant, In situ XRD analysis of the oxide layers formed by oxidation at 743 K on Zircaloy 4 and Zr–1NbO, J. Nucl. Mater. 280 (3) (2000) 318–330.
[7] F. Garzarolli, H. Seidel, R. Tricot, J. Gros, Oxide growth mechanism on zirconium alloys, in: Zirconium in the Nuclear Industry: 9th International Symposium, ASTM STP 1132, 1991, pp. 395–415.
[8] B. Cox, Some thoughts on the mechanisms of in-reactor corrosion of zirconium alloys, J. Nucl. Mater. 336 (2–3) (2005) 331–368.
[9] M. Preuss, P. Frankel, S. Lozano-Perez, D. Hudson, E. Polatidis, N. Ni, J. Wei, Studies regarding corrosion mechanisms in zirconium alloys, in: Zirconium in the Nuclear Industry – 16th International Symposium, vol. 8, no. 9, ASTM STP 1529, 2011, pp. 1–23.
[10] A. Garner, A. Gholinia, P. Frankel, M. Gass, I. MacLaren, M. Preuss, The microstructure and microtexture of zirconium oxide films studied by transmission electron backscatter diffraction and automated crystal orientation mapping with transmission electron microscopy, Acta Mater. 80 (2014) 159–171.
[11] M. Glavicic, Development and Application of Techniques for the Microstructural Characterisation of Hydrogen Permeability in Zirconium Oxides, McGill University, Montreal, 1998.
[12] A. Yilmazbayhan, E. Breval, A.T. Motta, R.J. Comstock, Transmission electron microscopy examination of oxide layers formed on Zr alloys, J. Nucl. Mater. 349 (3) (2006) 265–281.
[13] V.Y. Gertsman, A.P. Zhilyaev, J.A. Szpunar, Grain boundary misorientation distributions in monoclinic zirconia, Model. Simul. Mater. Sci. Eng. 5 (1997) 35–52.
[14] M. Elmosethi, B. Warr, S. McIntyre, A study of the hydrogen uptake mechanism in zirconium alloys, in: Zirconium in the Nuclear Industry: 10th International Symposium, ASTM STP 1245, 1994, pp. 62–79.
[15] N. Ramasubramanian, V. Perovic, M. Leger, Hydrogen transport in the oxide and hydrogen pickup by the metal during out- and in-reactor corrosion of Zr–2.5Nb pressure tube material, in: Zirconium in the Nuclear Industry: 12th International Symposium, ASTM STP 1354, 2000, pp. 853–876.
[16] J.A. Szpunar, W. Qin, H. Li, N.a.P. Kiran Kumar, Roles of texture in controlling oxidation, hydrogen ingress and hydride formation in Zr alloys, J. Nucl. Mater. 427 (1–3) (2012) 343–349.
[17] G. Sundell, M. Thuvander, A. Yatim, H. Nordin, H.-O. Andrén, Direct observation of hydrogen and deuterium in oxide grain boundaries in corroded zirconium alloys, Corros. Sci. 90 (2015) 1–4.
[18] N. Ni, S. Lozano-Perez, M. Jenkins, C. English, G.D. Smith, J. Sykes, C.R. Grovenor, Porosity in oxides on zirconium fuel cladding alloys, and its importance in controlling oxidation rates, Scr. Mater. 62 (8) (2010) 564–567.
[19] J. Lin, H. Li, J.A. Szpunar, Analysis of zirconium oxide formed during oxidation at 623 K on Zr–2.5Nb and Zircaloy-4, Mater. Sci. Eng., A 381 (1–2) (2004) 104–112.
[20] A. Garner, M. Preuss, P. Frankel, A method for accurate texture determination of thin oxide films by glancing angle laboratory X-ray diffraction, J. Appl. Crystallogr. 47 (2014) 575–583.
[21] N. Ni, D. Hudson, J. Wei, P. Wang, S. Lozano-Perez, G.D.W. Smith, J.M. Sykes, S.S. Yardley, K.L. Moore, S. Lyon, R. Cottis, M. Preuss, C.R.M. Grovenor, How the crystallography and nanoscale chemistry of the metal/oxide interface develops during the aqueous oxidation of zirconium cladding alloys, Acta Mater. 60 (20) (2012) 7132–7149.

[22] H. Li, M. Glavicic, J.A. Szpunar, A model of texture formation in ZrO_2 films, Mater. Sci. Eng., A 366 (1) (2004) 164–174.
[23] J. Lin, Effect of Texture and Microstructure of Zirconium Alloys on their Oxidation and Oxide Texture, McGill University, Montreal, Canada, 2005.
[24] J. Lin, H. Li, C. Nam, J.A. Szpunar, Analysis on volume fraction and crystal orientation relationship of monoclinic and tetragonal oxide grown on Zr–2.5Nb alloy, J. Nucl. Mater. 334 (2–3) (2004) 200–206.
[25] B. Wadman, Z. Lai, H.O. Andren, A.L. Nystrom, P. Rudling, H. Pettersson, Microstructure of oxide layers formed during autoclave testing of zirconium alloys, in: Zirconium in the Nuclear Industry: 10th International Symposium, ASTM STP 1245, 1994, pp. 579–598.
[26] W. Gong, H. Zhang, Y. Qiao, H. Tian, X. Ni, Z. Li, X. Wang, Grain morphology and crystal structure of pre-transition oxides formed on Zircaloy-4, Corros. Sci. 74 (2013) 323–331.
[27] H.G. Kim, J.Y. Park, B.K. Choi, Y.H. Jeong, Evaluation of pre-transition oxide on Zr–0.4 Nb alloy by using the HVEM, J. Nucl. Mater. 374 (1–2) (2008) 204–210.
[28] J. Wei, P. Frankel, M. Blat, A. Ambard, R.J. Comstock, L. Hallstadius, S. Lyon, R.A. Cottis, M. Preuss, Autoclave study of zirconium alloys with and without hydride rim, Corros. Eng., Sci. Technol. 47 (7) (2012) 516–528.
[29] a. Yilmazbayhan, Structure of zirconium alloy oxides formed in pure water studied with synchrotron radiation and optical microscopy: relation to corrosion rate, J. Nucl. Mater. 324 (1) (2004) 6–22.
[30] R.M. Langford, C. Clinton, In situ lift-out using a FIB-SEM system, Micron 35 (7) (2004) 607–611.
[31] N. Ni, Study of Oxidation Mechanisms of Zirconium Alloys by Electron Microscopy, University of Oxford, 2011.
[32] P.W. Trimby, Orientation mapping of nanostructured materials using transmission Kikuchi diffraction in the scanning electron microscope, Ultramicroscopy 120 (2012) 16–24.
[33] E.F. Rauch, M. Véron, Automatic crystal orientation and phase mapping in TEM by precession diffraction, Microsc. Anal. 22 (2008) S5–S8.
[34] E.F. Rauch, L. Dupuy, Rapid spot diffraction patterns identification through template matching, Arch. Metall. Mater. 50 (1) (2005) 87–99.
[35] A. Garner, Investigating the Effect of Oxide Texture on the Corrosion Performance of Zirconium Alloys, The University of Manchester, Manchester, 2015.
[36] Y. Takagawa, S. Ishimoto, Y. Etoh, T. Kubo, K. Ogata, O. Kubota, The correlation between microstructures and in-BWR corrosion behavior of highly irradiated Zr-based alloys, Zircon. Nucl. Ind. 14th Int. Symp. ASTM STP 1467, 2004, pp. 386–403.
[37] A. Couet, A.T. Motta, R.J. Comstock, R.L. Paul, Cold neutron prompt gamma activation analysis, a non-destructive technique for hydrogen level assessment in zirconium alloys, J. Nucl. Mater. 425 (1–3) (2012) 211–217.
[38] A. Couet, A.T. Motta, R.J. Comstock, Hydrogen pickup measurements in zirconium alloys: Relation to oxidation kinetics, J. Nucl. Mater. 451 (1–3) (2014) 1–13.
[39] A. Couet, Hydrogen pickup mechanism of zirconium alloys, The Pennsylvania State University, 2014.
[40] N. Ni, S. Lozano-Perez, J. Sykes, G.D. Smith, C.R. Grovenor, Focussed ion beam sectioning for the 3D characterisation of cracking in oxide scales formed on commercial ZIRLO™ alloys during corrosion in high temperature pressurised water, Corros. Sci. 53 (12) (2011) 4073–4083.
[41] R. Hielscher, H. Schaeben, D. Chateigner, On the entropy to texture index relationship in quantitative texture analysis, J. Appl. Crystallogr. 40 (2) (2007) 371–375.
[42] F. Bachmann, R. Hielscher, H. Schaeben, Texture analysis with MTEX – free and open source software toolbox, Solid State Phenom. 160 (2010) 63–68.
[43] P. Bossis, G. Lelikvre, P. Barberis, X. Iltis, F. Lefebvre, Multi-scale characterization of the metal-oxide interface of zirconium alloys, in: Zirconium in the Nuclear Industry: 12th International Symposium, ASTM STP 1354, 2000, pp. 918–945.
[44] P. Tejland, H.-O. Andrén, Origin and effect of lateral cracks in oxide scales formed on zirconium alloys, J. Nucl. Mater. 430 (1–3) (2012) 64–71.
[45] E. Polatidis, P. Frankel, J. Wei, M. Klaus, R.J. Comstock, A. Ambard, S. Lyon, R. Cottis, M. Preuss, Residual stresses and tetragonal phase fraction characterisation of corrosion tested Zircaloy-4 using energy dispersive synchrotron X-ray diffraction, J. Nucl. Mater. 432 (1–3) (2013) 102–112.
[46] V.Y. Gertsman, Y.P. Lin, A.P. Zhilyaev, J.A. Szpunar, Special grain boundaries in zirconia corrosion films, Philos. Mag. A 79 (7) (1999) 1567–1590.
[47] E.C. Subbarao, Martensitic transformation in zirconia, Phys. Status Solidi 9 (1974).
[48] J. Godlewski, J. Gros, M. Lambertin, J. Wadier, H. Weidinger, Raman spectroscopy study of the tetragonal-to-monoclinic transition in zirconium oxide scales and determination of overall oxygen diffusion by nuclear analysis of O(18), in: Zirconium in the Nuclear Industry: 9th International Symposium. ASTM STP 1132, 1991, pp. 416–436.
[49] A.T. Motta, A. Yilmazbayhan, R.J. Comstock, J. Partezana, G.P. Sabol, B. Lai, Z. Cai, Microstructure and growth mechanism of oxide layers formed on Zr alloys studied with micro-beam synchrotron radiation, in: Zirconium in the Nuclear Industry: 14th International Symposium, vol. 2, no. 5, ASTM STP 1467, 2005, pp. 205–232.
[50] H. Hulme, M. Preuss, S. Lyon, A. Steuwer, K. Noren, S. Carlson, M. Gass, M. Ivermark, and R. J. Comstock, A X-ray absorption near-edge structure (XANES) study of the Sn L3 edge in a Zircaloy-4 oxide film, Submitt. to Thin Solid Film, 2014.
[51] S. Fabris, A.T. Paxton, M.W. Finnis, A stabilization mechanism of zirconia based on oxygen vacancies only, Acta Mater. 50 (2002) 5171–5178.
[52] Y.S. Kim, Y.H. Jeong, J.N. Jang, Stress measurements during thin film zirconium oxide growth, J. Nucl. Mater. 412 (2) (2011) 217–220.
[53] D. Pecheur, V. P. Filippov, A. B. Bateev, and J. J. Ivanov, Mössbauer investigations of the chemical states of tin and iron atoms in zirconium alloy oxide film, in: Zircon. Nucl. Ind. 13th Int. Symp. ASTM STP 1423, 2002, pp. 135–153.
[54] B.D.C. Bell, S.T. Murphy, P.A. Burr, R.W. Grimes, M.R. Wenman, Accommodation of Tin in Tetragonal ZrO_2, Submitt. to J. Appl. Phys., 2015.
[55] E.R. Bradley, A.-L. Nyström, Microstructure and properties of corrosion-resistant zirconium-tin-iron- chromium-nickel alloys, in: Zirconium in the Nuclear Industry: 10th International Symposium, ASTM STP 1245, 1994, pp. 483–498.
[56] P. Bossis, F. Lefebvre, P. Barberis, A. Galerie, Corrosion of zirconium alloys: link between the metal/oxide interface roughness, the degradation of the protective oxide layer and the corrosion kinetics, Mater. Sci. Forum 369–372 (2001) 255–262.
[57] S. Yardley, K. Moore, N. Ni, J. Wei, S. Lyon, M. Preuss, S. Lozano-Perez, C.R.M. Grovenor, An investigation of the oxidation behaviour of zirconium alloys using isotopic tracers and high resolution SIMS, J. Nucl. Mater. 443 (1–3) (2013) 436–443.